

AperTO - Archivio Istituzionale Open Access dell'Università di Torino

## Engineered MoxC/TiO<sub>2</sub> interfaces for efficient noble metal-free photocatalytic hydrogen production

### This is the author's manuscript

*Original Citation:*

*Availability:*

This version is available <http://hdl.handle.net/2318/1886730> since 2023-01-23T09:58:46Z

*Published version:*

DOI:10.1016/j.apcatb.2022.121783

*Terms of use:*

Open Access

Anyone can freely access the full text of works made available as "Open Access". Works made available under a Creative Commons license can be used according to the terms and conditions of said license. Use of all other works requires consent of the right holder (author or publisher) if not exempted from copyright protection by the applicable law.

(Article begins on next page)

# Engineered $\text{Mo}_x\text{C}/\text{TiO}_2$ interfaces for efficient noble metal-free photocatalytic hydrogen production

Yan Wang<sup>a,b</sup>, Lorenzo Mino<sup>c\*</sup>, Francesco Pellegrino<sup>c</sup>, Narcís Homs<sup>a,b</sup>, Pilar Ramírez de la Piscina<sup>a\*</sup>

<sup>a</sup>Departament de Química Inorgànica i Orgànica, secció de Química Inorgànica & Institut de Nanociència i Nanotecnologia (IN2UB), Universitat de Barcelona, Martí i Franquès 1, 08028 Barcelona, Spain

<sup>b</sup>Catalonia Institute for Energy Research (IREC), Jardins de les Dones de Negre 1, 08930 Barcelona, Spain.

<sup>c</sup>Department of Chemistry and NIS Centre, University of Torino, via Giuria 7, 10125 Torino, Italy.

\*Corresponding authors e-mail addresses: [lorenzo.mino@unito.it](mailto:lorenzo.mino@unito.it); [pilar.piscina@qi.ub.edu](mailto:pilar.piscina@qi.ub.edu)

## Abstract

Photoinduced hydrogen production is a promising green strategy to store the power from the Sun as chemical energy. One major challenge is to obtain efficient photocatalytic systems without employing noble metals. In this contribution we combine different shape-controlled bipyramidal or nano-sheet anatase  $\text{TiO}_2$  nanoparticles, preferentially exposing {101} or {001} facets, and  $\text{Mo}_x\text{C}$  as co-catalyst to realize noble metal-free photocatalysts. The effect of  $\text{TiO}_2$  morphology on the functional properties and efficiency of the final composite materials in the photocatalytic  $\text{H}_2$  production is carefully assessed combining powder X-ray diffraction, transmission electron microscopy, X-ray photoelectron spectroscopy, UV-Vis diffuse reflectance spectroscopy, photoluminescence, transient photocurrent and electrochemical impedance spectroscopy. Engineered  $\text{Mo}_x\text{C}/\text{TiO}_2$  interfaces, which exploit the superior reducing ability of the anatase (101) surface, result to be particularly active in the photocatalytic  $\text{H}_2$  production from ethanol aqueous solutions.

## Keywords

Green hydrogen, ethanol photoreforming, nanoparticle shape-engineering, transition metal carbides

## 1. Introduction

The harnessing of solar radiation for energy purposes is a crucial step for a sustainable future and its efficient storage is one of the major challenges. In this respect, hydrogen is a promising energy vector to store the power from the Sun as chemical energy. Moreover, H<sub>2</sub> is an enabling molecule for the production of ammonia, carbon-based fuels and chemicals. For these reasons, in the last years huge research efforts have been devoted to improve the efficiency of photocatalytic water splitting and organics photoreforming processes, which allow obtaining clean hydrogen [1, 2].

In this scenario, TiO<sub>2</sub> is a key photoactive semiconductor and different studies tried to improve its performance by controlling its crystal structure, particle size, surface properties and morphology [3-5]. In particular, shape-engineering has recently emerged as a powerful tool to optimize the NPs physicochemical properties [6, 7]. Concerning the anatase TiO<sub>2</sub> crystalline phase, the use of suitable capping agents (e.g. fluorides) allows obtaining NPs which preferentially expose {001} facets [8], which are usually considerably less stable than the {101} ones [9]. The different NP morphology can have a strong impact on the material surface properties [10-12] and, hence, on its functional performance [13-15]. For instance, it has been reported that {101} facets favour the electron (e<sup>-</sup>) transfer from the metal oxide to water, accelerating the rate of hydrogen photoproduction [16]. Conversely, holes (h<sup>+</sup>) should preferentially migrate toward {001} facets where the oxidation processes should take place [16]. Since a suitable balance between the oxidation and reduction reactions is needed, many researchers tried to find the best combination of different anatase TiO<sub>2</sub> facets to maximize charge separation and, thus, photocatalytic activity [17-21]. However, this issue is still matter of a lively debate in literature.

Another important aspect is the surface modification of the TiO<sub>2</sub> NPs by addition of co-catalysts to improve the charge carrier separation and to facilitate the H<sub>2</sub> photocatalytic production. For this purpose, Pt, Ag, Pd or Au NPs are the most employed materials [3, 22]. The addition of noble metals to the semiconductor, decreases the H<sub>2</sub>-evolution overpotential and contributes to the suppression of recombination between h<sup>+</sup> and e<sup>-</sup>. However, huge research efforts are devoted to develop noble-metal-free co-catalysts [23]. Transition metal

carbides such as  $\text{Mo}_x\text{C}$  and  $\text{W}_x\text{C}$ , are known to display versatile catalytic properties, similar to the Pt-group elements, being stable, cheaper and with the advantage of the abundance of Mo and W [24-27]. In this context,  $\text{Mo}_x\text{C}$  and  $\text{W}_x\text{C}$  have been widely studied as catalysts for different electrochemical and chemical processes and they are considered promising candidates to be used as co-catalysts in the photocatalytic hydrogen production [28-33]. Indeed, the presence of  $\text{Mo}_x\text{C}$  or  $\text{W}_x\text{C}$  on the surface of the semiconductor, can favor the transfer of the photogenerated  $e^-$  to the  $\text{H}^+$ , and therefore the  $\text{H}_2$  generation. Moreover, the creation of heterojunctions can have a positive effect, as demonstrated in the case of WC- $\text{Mo}_2\text{C}$  for the photocatalytic hydrogen production from methanol solutions [34]. Interestingly, also  $\text{MoC-Mo}_2\text{C}$  heterostructures have shown a synergistic effect improving the electrocatalytic  $\text{H}_2$  evolution reaction [35].

Based on the literature results discussed above, in this work, we decided to combine shape-controlled  $\text{TiO}_2$  NPs with molybdenum carbide, containing both  $\text{MoC}$  and  $\text{Mo}_2\text{C}$  phases, as co-catalyst, to obtain an efficient noble-metal-free photocatalyst for hydrogen production. In particular, we compare three different kinds of shape-engineered anatase  $\text{TiO}_2$  NPs with different  $\{101\}/\{001\}$  facet ratio, ranging from 0.3 to 9. The deposition of previously synthesized  $\text{Mo}_x\text{C}$ , onto shape-engineered anatase  $\text{TiO}_2$  NPs allowed us to report, for the first time, the co-catalyst effect of  $\text{Mo}_x\text{C}$  as a function of the anatase  $\text{TiO}_2$  NPs shape. The samples were tested in the photocatalytic hydrogen production from ethanol aqueous solutions since biomass-derived ethanol is the biofuel produced in the largest amount worldwide and, thus, it is considered a promising renewable feedstock for  $\text{H}_2$  production using catalytic reforming technologies [36, 37].

## 2. Experimental

### 2.1 Materials synthesis

**$\text{TiO}_2$  nano-sheets ( $\text{TiO}_2(\text{NS})\text{-F}$ ).** The synthesis of  $\text{TiO}_2$  nano-sheets was performed by a solvothermal method, following an established literature procedure [38]. In a typical synthesis, 25 ml  $\text{Ti}(\text{O}i\text{Bu})_4$  (Aldrich reagent grade 97%) was poured into a Teflon lined stainless steel reactor and 3.5 ml of concentrated hydrofluoric acid (Aldrich reagent grade

47%) was added dropwise under stirring. The reactor was sealed and kept under stirring at 250 °C for 24 hours. The resulting paste was centrifuged and washed several times with acetone to remove the residual organics and then with water (Milli-Q). The final aqueous suspension was freeze-dried obtaining a bluish powder (the color is due to F<sup>-</sup> doping).

**Thermally treated TiO<sub>2</sub> nano-sheets (TiO<sub>2</sub>(NS)-600).** For a complete removal of the fluorides from the nanoparticles, the as-synthesized (TiO<sub>2</sub>(NS)-F) nano-sheets were heated at 600 °C for 1 hour in air (heating ramp 6 °C min<sup>-1</sup>). The resulting powder was white.

**TiO<sub>2</sub> bipyramids (TiO<sub>2</sub>(bipy)).** The synthesis of TiO<sub>2</sub> truncated bipyramids was obtained, employing an already well-established procedure [39, 40], by forcing the hydrolysis of a 65 mM aqueous solution of Ti(TEOAH)<sub>2</sub> complex (TEOAH = triethanolamine; initial pH 10) by a hydrothermal treatment at 220 °C for 50 hours in autoclave. TEOAH was used also as capping agent to induce the growth of the (101) surface. The material was then heated at 600 °C for 1 hour in air atmosphere (heating ramp of 6 °C min<sup>-1</sup>).

**Mo<sub>x</sub>C nanoparticles.** Mo<sub>x</sub>C was synthesized using a novel sol-gel method, based on a procedure previously developed by some of us [41]. MoCl<sub>5</sub> (Aldrich reagent grade 95%) and 4,5 dicyanoimidazole (DI) (Aldrich reagent grade 99%) were used as metal and carbon sources, respectively. In brief, 5.6 mmol of MoCl<sub>5</sub> and 2.8 mmol of DI were added into a 15 mL of ethanol under stirring. Afterwards, the sample was treated at 60 °C in an oven under air and a gel was formed. The gel was then treated under Ar flow in a tubular reactor, with an increase of temperature of 2.5 °C·min<sup>-1</sup>, up to 700 °C. The system was kept at 700 °C under Ar flow for 5 h, and then it was cooled down to room temperature.

**Mo<sub>x</sub>C/TiO<sub>2</sub> photocatalysts.** TiO<sub>2</sub> NPs and the required amount of Mo<sub>x</sub>C for obtaining a Mo content of about 1 %wt, were dispersed in ethanol and treated under Ar flow with ultrasounds (SONICS VCX 500) at 30 °C for 1 h and 250 W. Then, ethanol was carefully evaporated under continuous stirring at 50 °C under Ar flow. The photocatalysts were labelled Mo<sub>x</sub>C/TiO<sub>2</sub>(NS)-X (X = F, 600) and Mo<sub>x</sub>C/TiO<sub>2</sub>(bipy).

Commercial (Degussa (Evonik)) Aeroxide TiO<sub>2</sub> P25 was used as reference material (TiO<sub>2</sub> P25).

## 2.2 Characterization

The Mo content in the samples was determined by inductively coupled plasma atomic emission spectrometry using a Perkin Elmer Optima 3200RL equipment.

N<sub>2</sub> adsorption–desorption isotherms were recorded at -196 °C using a Micromeritics Tristar II 3020 equipment. Samples were previously degassed under Ar flow at 100 °C. The specific surface area ( $S_{\text{BET}}$ ) was calculated by multipoint Brunauer Emmet Teller (BET) analysis of the adsorption isotherms.

Powder X-ray diffraction (XRD) patterns of the prepared samples were recorded using a PANalytical X'Pert PRO MPD Alpha1 powder diffractometer equipped with Cu K $\alpha$ 1 radiation ( $\lambda=1.5406$  Å) at 45 kV – 40 mA with a X'Celerator Detector (Active length = 2.122°) in the range of 2 $\theta$  scan 10–100° with a step size of 0.017° and counting time of 80 s per step. A semiquantitative phase analysis was performed in as synthesized Mo<sub>x</sub>C nanoparticles, using accurate area intensities and the reference intensity ratios in the corresponding powder diffraction file [42]. The crystallite sizes were calculated using the Scherrer equation. The scanning electron microscopy (SEM) images of the pure TiO<sub>2</sub> nanoparticles were collected with a SEM of type Zeiss Supra 40, equipped with a Schottky field emitter and operating at 10 kV. SEM-EDX maps were acquired employing a FESEM TESCAN S9000G. The high-resolution transmission electron microscopy (HR-TEM) of Mo<sub>x</sub>C/TiO<sub>2</sub>-(NS)-X and Mo<sub>x</sub>C/TiO<sub>2</sub>-(bipy) samples were acquired on a JEOL JEM-2100 working at 200 kV.

The characterization by X-ray photoelectron spectroscopy (XPS) was performed using a Perkin Elmer PHI-5500 Multitechnique System with a hemispherical electron energy analyser and a 1486.6 eV Al K $\alpha$  radiation. The adventitious C 1s peak at 284.8 eV, which was previously determined in the same equipment using Au as reference, was taken as reference of binding energy values. Deconvolution of XPS peaks was carried out using the MultiPak XPS software.

UV–vis diffuse reflectance spectroscopy (UV-vis DRS) was performed using a Perkin Elmer Lambda 950 UV-vis Spectrometer with a 3 nm slit width and a speed of 655 nm min<sup>-1</sup>; BaSO<sub>4</sub> was used as reference. Band-gap values were determined from the corresponding Tauc plot and the approach reported in [43].

Photoluminescence (PL) measurements were obtained at room temperature using a Jobin-Yvon LabRam HR 800 dispersive spectrometer, coupled to an optical microscope Olympus BXFM (40× NUV microscope objective). The CCD detector was cooled at -70 °C. The employed excitation laser line was at 325 nm and the dispersive grating was 300 lines/mm. The transient photocurrent and the electrochemical impedance spectroscopy (EIS) measurements were carried out using a computer-controlled potentiostat (VMP3, BioLogic Science Instruments) with an undivided three-electrode cell. The counter electrode, reference electrode, and working electrodes were a Pt wire, a Ag/AgCl (3 M KCl) electrode, and the photocatalyst electrode (1 cm<sup>2</sup> geometric area), respectively; a 0.5 M Na<sub>2</sub>SO<sub>4</sub> aqueous solution was used as electrolyte. EIS measurements were carried out in the frequency range of 100 kHz to 0.1 Hz. Measurements under illumination were performed using a 150 W AM 1.5G solar simulator (Solar Light Co., 16S-300-002 v 4.0) with an incident light intensity set at 1 Sun (100 mW cm<sup>-2</sup>).

### **2.3 Photocatalytic hydrogen production experiments**

The tests were carried out at atmospheric pressure and 20 °C in a jacketed glass reactor designed for continuous gas flow operation and equipped with a condenser, kept at -20 °C, at the outlet. A broad-spectrum UV-visible Hg lamp (Ace-Hanovia, maximum power at  $\lambda=366$  nm, emission spectrum shown in Figure S1), was placed inside the reactor in a water-cooled jacket. For all the experiments, 250 mg of the photocatalyst, previously degassed under vacuum at 100 °C, and 250 mL of an ethanol<sub>(aq)</sub> (25 % v/v) solution, previously purged with Ar, were employed. After 30 min of stirring under dark and N<sub>2</sub>/Ar flowing, the solution was irradiated and, after 10 min of light on, the evolved gaseous products were periodically sampled at the outlet and on-line analysed using a Varian CP-4900 micro gas chromatograph provided with micro TCD detectors and two modules equipped with 10 m PPQ (He carrier) and 10 m molecular sieve 5Å (Ar carrier) columns, detection limit for H<sub>2</sub>, 50 ppm. The filtered liquid products were separately analyzed by gas chromatography at the end of the photocatalytic test (4 h) in a Bruker 450 GC equipment, with CP-Sil 8 CB and WAX columns and a FID detector.

For the reusability test, once the first photocatalytic test ended, the light and stirring were switched off. After that, the reactor was flushed with argon and kept under argon atmosphere, in dark, overnight. Then, a second photocatalytic test under the same experimental conditions was carried out.

### 3. Results and discussion

#### 3.1 Structural, morphological and chemical characterization of the TiO<sub>2</sub> and Mo<sub>x</sub>C/TiO<sub>2</sub> nanoparticles

As stated in the experimental section, three pure anatase materials with shape-controlled nanoparticles were synthesized following well established methods [39, 44]. Representative SEM images of the shape-controlled TiO<sub>2</sub> nanoparticles are reported in Figure 1. As visible in Figure 1A, the TiO<sub>2</sub>(NS)-F sample is composed of nanosheets, this sample was synthesized in the presence of fluorides as shape controllers and, therefore, mainly exposes the {001} facets (~ 80%) and only ~ 20% of the {101} one (for the details of the calculations of the percentage of exposed facets see Table S1 and Figure S2 in the Supporting Information). As highlighted in previous studies [39, 44], in which a more detailed morphological and surface characterization is reported, these NPs contain fluorides both adsorbed on the surface and in their bulk.

Calcination in air at 600 °C of TiO<sub>2</sub>(NS)-F NPs results in the TiO<sub>2</sub>(NS)-600 sample, which still shows a nanosheet shape (Figure 1B), but it is completely free from fluorides as it has been previously verified by combined TOF-SIMS, XPS, SEM-EDX, AES analyses [44]. However, the thermal treatment induces a sintering between pair of platelets, occurring through their basal (001) surfaces (Table 1), and, therefore, a decrease in the BET specific surface area and in the relative abundance of the {001} facets, accounting now for ~ 60% of the exposed terminations, occurs [44, 45].

Finally, TiO<sub>2</sub>(bipy) (Figure 1C), obtained without the use of fluorides, exhibit a bipyramidal shape which is dominated by {101} facets (90%) [44]. Its BET specific surface area is in-between those of TiO<sub>2</sub>(NS)-F and TiO<sub>2</sub>(NS)-600 samples (Table 1).

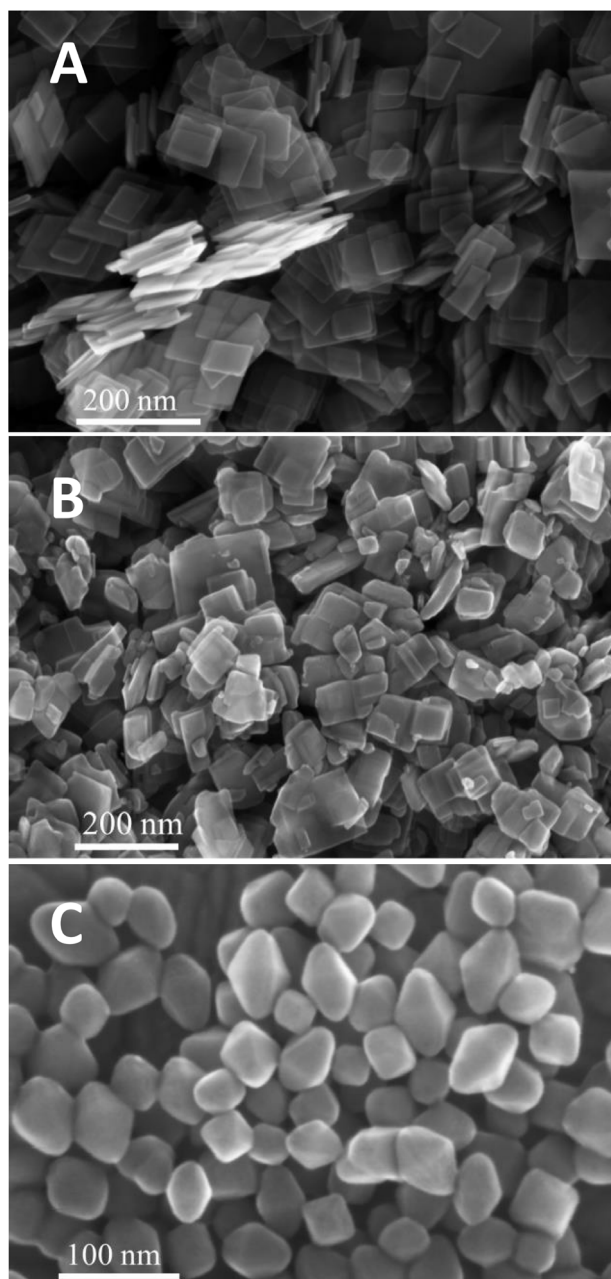


**Figure 1.** SEM images of  $\text{TiO}_2(\text{NS})\text{-F}$  (A),  $\text{TiO}_2(\text{NS})\text{-600}$  (B) and  $\text{TiO}_2(\text{bipy})$  (C) samples.

**Table 1.** Main characteristics of pure and Mo<sub>x</sub>C-loaded TiO<sub>2</sub> samples: average dimension of crystal domains obtained by Scherrer analysis of the 004 and 200 XRD peaks; BET specific surface area; Mo content; bandgap energy values.

Catalyst	d <sub>004</sub> (nm)	d <sub>200</sub> (nm)	BET SSA (m <sup>2</sup> /g)	Mo content (wt%)	Bandgap (eV)
TiO <sub>2</sub> (NS)-F	13	54	36	--	3.27
TiO <sub>2</sub> (NS)-600	31	53	20	--	3.25
TiO <sub>2</sub> (bipy)	40	31	27	--	3.10
Mo <sub>x</sub> C/TiO <sub>2</sub> (NS)-F	14	56	26	0.96	3.27
Mo <sub>x</sub> C/TiO <sub>2</sub> (NS)-600	30	53	9	0.73	3.26
Mo <sub>x</sub> C/TiO <sub>2</sub> (bipy)	36	29	15	0.69	2.92

X-ray diffraction (Figure 2) was employed to verify the crystal phase of the TiO<sub>2</sub> NPs, which was confirmed to be pure anatase (ICDD PDF 00-021-1272) for all materials. Concerning the XRD pattern of pure Mo<sub>x</sub>C NPs (bottom part of Figure 2 and Figure S3), we can identify the characteristic XRD peaks of the hexagonal Mo<sub>2</sub>C (ICDD PDF 04-014-1517) and cubic MoC (ICDD PDF 04-003-1480) phases. A semiquantitative phase analysis was performed by carefully fitting the XRD peaks of the two phases and considering the reference intensity ratios in the corresponding powder diffraction file [42]. The phase distribution in pure Mo<sub>x</sub>C NPs was found to be of about 14% of hcp Mo<sub>2</sub>C and 86% of fcc MoC with average crystallite sizes of 11 nm and 4 nm for hcp Mo<sub>2</sub>C and fcc MoC, respectively.

In the patterns of the different Mo<sub>x</sub>C/TiO<sub>2</sub> samples (Figure 2), only characteristic anatase peaks were found. It was not possible to find XRD signals of molybdenum carbides or other Mo-containing phases owing to the low Mo content, which was in the 0.7-1 % wt/wt range (see Table 1).

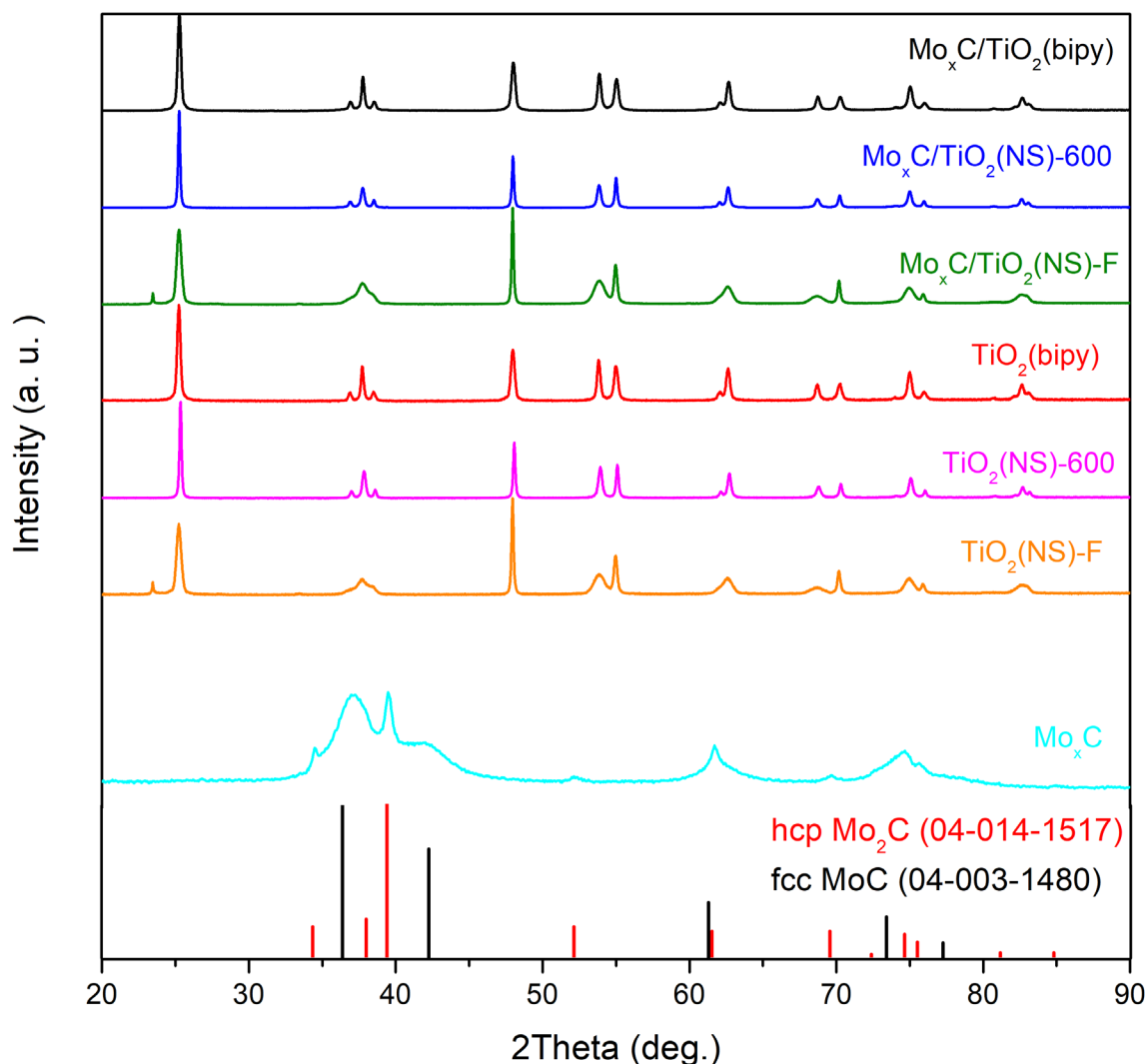


**Figure 2.** XRD patterns of the pure and Mo<sub>x</sub>C loaded TiO<sub>2</sub> samples. Reference hcp Mo<sub>2</sub>C and fcc MoC patterns are also reported.

The composite materials were studied also by TEM, which confirmed that the molybdenum carbide deposition does not significantly modify the TiO<sub>2</sub> bipyramids and nano-sheet morphology (Figure 3A, C and E). High resolution images (Figure 3B, D and F) allow visualizing small particles of Mo<sub>x</sub>C co-catalyst, which resulted to be well dispersed on the TiO<sub>2</sub> surfaces, as confirmed also by the SEM-EDX analysis performed on the Mo<sub>x</sub>C/TiO<sub>2</sub>(bipy) sample (Figure S4). As visible in the histograms reported in Figure 3, in all cases, a bimodal particle size distribution was observed: small Mo<sub>x</sub>C NPs with a mean size

of about 4-6 nm and less abundant and bigger  $\text{Mo}_x\text{C}$  NPs (11-12 nm) were found. This result is in agreement with the phase distribution determined by XRD for the  $\text{Mo}_x\text{C}$  NPs used in the preparation of  $\text{Mo}_x\text{C}/\text{TiO}_2$  samples; small  $\text{Mo}_x\text{C}$  NPs could correspond to fcc MoC and bigger  $\text{Mo}_x\text{C}$  NPs to hcp  $\text{Mo}_2\text{C}$ . Despite we cannot unequivocally identify from the present TEM results, the corresponding phase of each domain of particle size, a recent study on the nanoparticle size effects for molybdenum and tungsten carbides highlights that the fcc phases are prevalent at small particles sizes, while hexagonal phases tend to dominate the large particle size regions [46], supporting our interpretation of the XRD and TEM results.

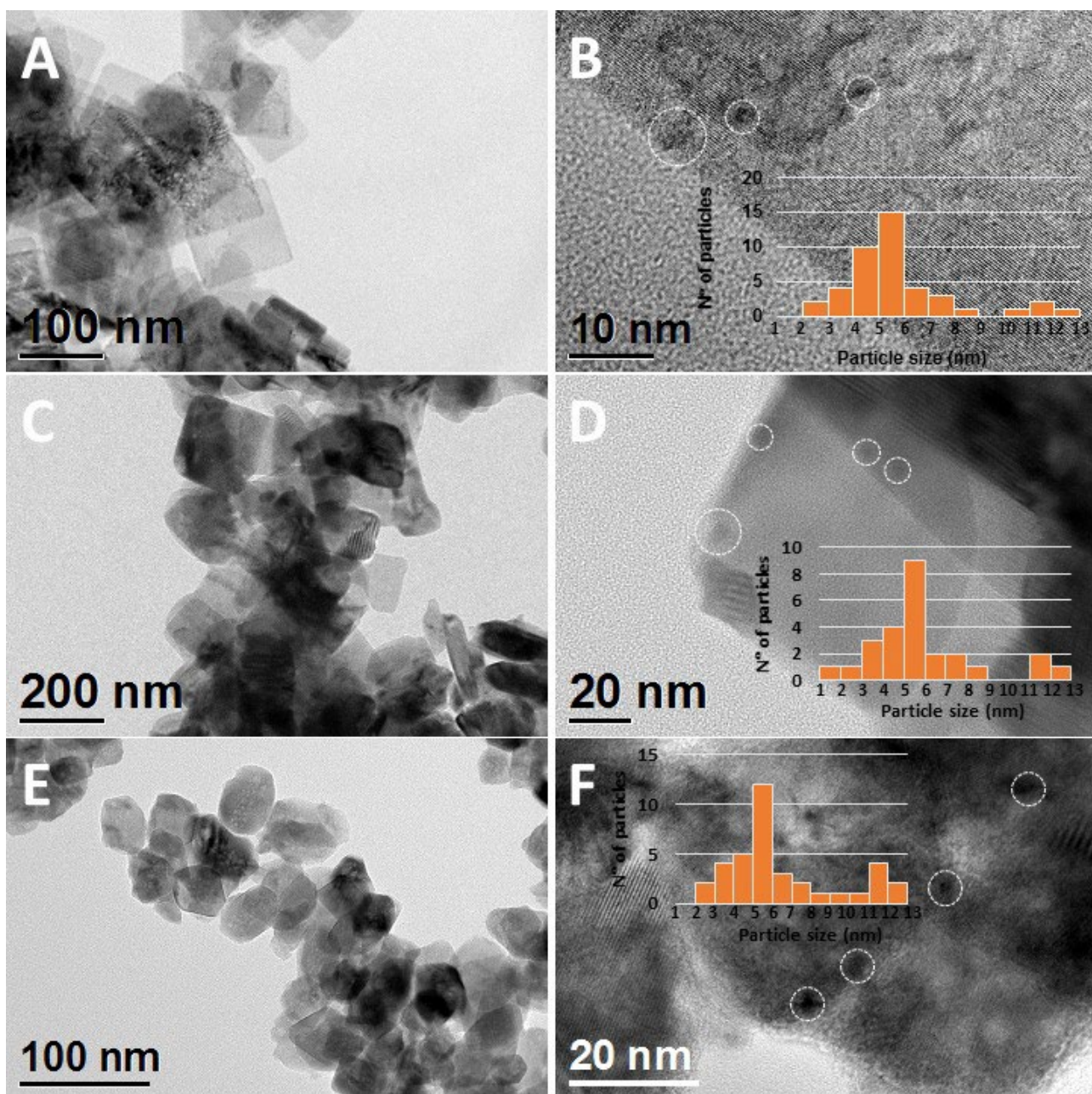


**Figure 3.** TEM and HR-TEM images of samples: A) and B) Mo<sub>x</sub>C/TiO<sub>2</sub>(NS)-F; C) and D) Mo<sub>x</sub>C/TiO<sub>2</sub>(NS)-600; E) and F) Mo<sub>x</sub>C/TiO<sub>2</sub>(bipy). White circles highlight the Mo<sub>x</sub>C particles. The inset histograms show the Mo<sub>x</sub>C particle size distribution for the different samples.

Mo<sub>x</sub>C-containing materials were characterized by X-ray photoelectron spectroscopy (see survey spectra in Figure S5). Figure 4 shows the corresponding Mo 3d high resolution spectrum, which is characterized by the presence of two main broad components at 232.0-231.7 eV and 235.1-234.9 eV, ascribed to the Mo 3d<sub>5/2</sub> and Mo 3d<sub>3/2</sub> levels in Mo<sup>5+</sup> species [47]. The doublet at 228.7-228.3 and 231.8-231.4 eV is due to the presence of Mo<sup>2+</sup> and/or Mo<sup>3+</sup>, likely related to Mo<sub>2</sub>C and/or oxycarbide species [31, 47]. Moving to the C 1s spectrum (Figure S6), its deconvolution shows for all samples a main component ascribed to C–C (at 284.8 eV) and minor components characteristics of C–O (at 286.9-286.6 eV) and O=C–O (at 288.5 eV) species [41]. Interestingly, the Mo<sub>x</sub>C/TiO<sub>2</sub>(bipy) sample shows also an additional shoulder at 283.0 eV, assigned to Mo–C bonds [48]. Moreover, the composite material based on bipyramidal TiO<sub>2</sub> NPs is different from the nanosheet TiO<sub>2</sub>-based samples also in the Ti 2p spectrum (Figure 4) since the expected Ti<sup>4+</sup> 2p<sub>3/2</sub> peak at 458.8 eV is associated with a shoulder at 457.5 eV attributed to Ti<sup>3+</sup> species [49]. O 1s spectra show in all cases a main band with maximum at about 530 eV characteristic of surface oxide of TiO<sub>2</sub> and a shoulder at higher BE which is related with molybdenum oxide or oxycarbide species (Figure S7). On the other hand, the shoulder with maximum at 528.4 eV in the O 1s spectrum of Mo<sub>x</sub>C/TiO<sub>2</sub>(bipy) could be related with the presence of Ti<sup>3+</sup> [50]. Therefore, the XPS data show that the deposition of the carbide phase on TiO<sub>2</sub> induces a preferential reduction of the surface Ti<sup>4+</sup> to Ti<sup>3+</sup> in bipyramidal anatase NPs, which mainly expose {101} facets. This finding can be explained considering the different barriers for oxygen vacancy migration reported for the (101) with and (001) surfaces [51], which result in a different reducibility of the two crystal facets. Finally, we consider the F 1s core level spectra (Figure S8) which confirm that some fluorides are still present on the surface of Mo<sub>x</sub>C/TiO<sub>2</sub>(NS)-F NPs even after the ultrasound-assisted procedure performed to load the molybdenum carbide phase.

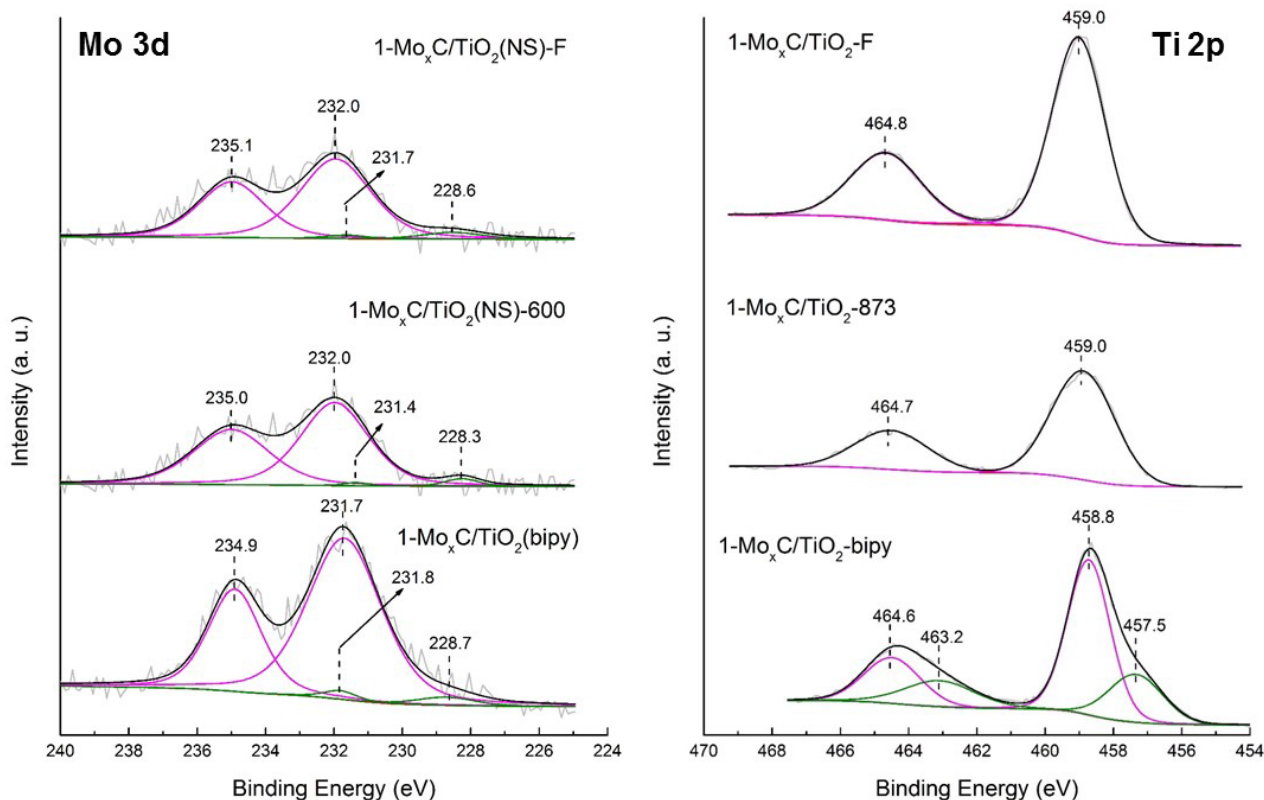


**Figure 4.** Mo 3d (left) and Ti 2p (right) XPS spectra of Mo<sub>x</sub>C/TiO<sub>2</sub>(NS)-X and Mo<sub>x</sub>C/TiO<sub>2</sub>(bipy) samples.

From the UV-vis spectroscopy analysis, we calculated the band gap values (Table 1) using the corresponding Tauc plots (Figure S9). Considering pristine TiO<sub>2</sub> NPs, the TiO<sub>2</sub>(bipy) sample shows the smallest band gap (3.10 eV). This observation seems to be in contradiction with previous data on micrometric crystals and with first principles calculations which suggested a smaller band gap for crystal terminated by the (001) surface [14]. However, it should be considered that the particle thickness along the *c*-axis for the nanosheet NPs is around 10 nm (Table S1), while it is about 40 nm for TiO<sub>2</sub>(bipy), hence for TiO<sub>2</sub>(NS) quantum confinement effects could start to be relevant, leading to an increase of the energy gap [52]. Moving now to the composite materials, we can see that for the Mo<sub>x</sub>C/TiO<sub>2</sub>(NS) samples the addition of molybdenum carbide does not modify the band gap. Conversely, in the Mo<sub>x</sub>C/TiO<sub>2</sub>(bipy) system we observe a slight further decrease of the band gap from 3.10 to 2.92 eV, which can be correlated with the different surface chemistry and

the formation of  $\text{Ti}^{3+}$  species highlighted by the XPS analysis.

### **3.2 Photoelectrochemical properties and photocatalytic hydrogen production**

The photoelectrochemical properties of samples were determined combining photoluminescence (PL), electrochemical impedance spectroscopy (EIS) and transient photocurrent measurements.  $\text{TiO}_2$  PL emission spectrum accounts for the photoinduced charge recombination and can be related with  $\text{TiO}_2$  photoactivity [53]. Besides the structure and morphology of  $\text{TiO}_2$  nanoparticles, the adsorbates onto the  $\text{TiO}_2$  surface determine the PL spectrum [54]. Figure 5 shows the PL spectra of all the materials prepared. In all cases, wide PL bands with maxima at about 595 nm were found, which are related to the presence of a high density of defect sites [55]. In particular, a component at about 495-540 nm has been associated with the presence of surface oxygen vacancies and one around 600-650 nm with subsurface oxygen vacancies [56]. It is worth noting that the intensity of PL bands, which depends on the recombination rate of photoinduced charges [57], follows the trend:  $\text{TiO}_2(\text{NS})\text{-F} \gg \text{TiO}_2(\text{NS})\text{-600} > \text{TiO}_2(\text{bipy}) > \text{Mo}_x\text{C}/\text{TiO}_2(\text{NS})\text{-F} > \text{Mo}_x\text{C}/\text{TiO}_2(\text{NS})\text{-600} > \text{Mo}_x\text{C}/\text{TiO}_2(\text{bipy})$  (Figure 5). In particular, the calcination of  $\text{TiO}_2(\text{NS})\text{-F}$  at 600 °C led to a marked decrease of the intensity of PL band indicating a lower electron/hole recombination kinetics. In all cases,  $\text{Mo}_x\text{C}$ -containing samples exhibited PL bands with lower intensity than the corresponding  $\text{TiO}_2$ : this indicates a main role of  $\text{Mo}_x\text{C}$  in hindering the electron/hole recombination, which is expected to be reflected in the photocatalytic behavior of materials containing  $\text{Mo}_x\text{C}$ .

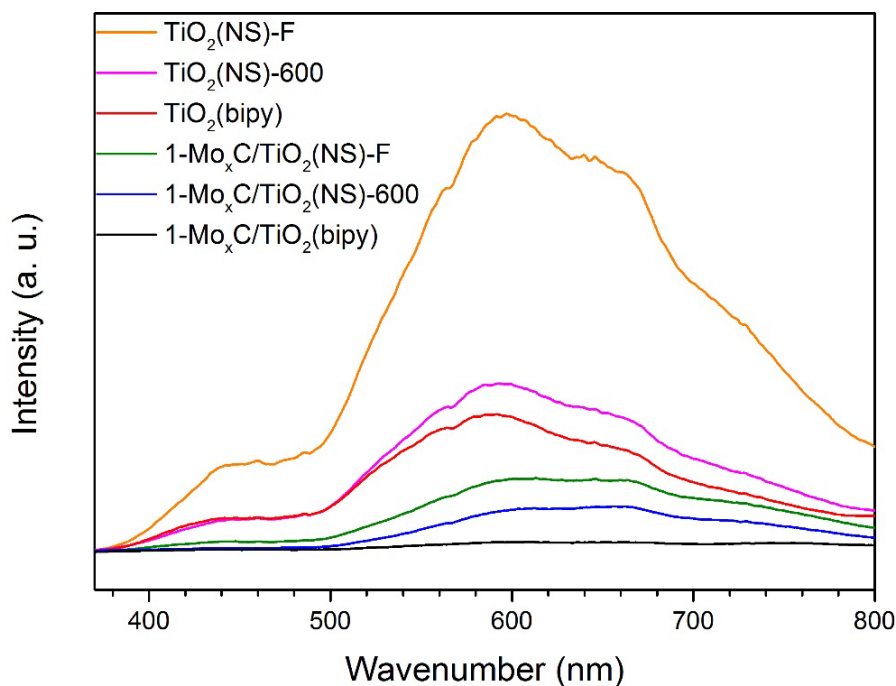


**Figure 5.** Photoluminescence spectra of  $\text{Mo}_x\text{C}/\text{TiO}_2(\text{NS})\text{-X}$ ,  $\text{Mo}_x\text{C}/\text{TiO}_2(\text{bipy})$ ,  $\text{TiO}_2(\text{NS})\text{-X}$  and  $\text{TiO}_2(\text{bipy})$  samples.

The transient photocurrent response of samples was determined using on/off pulses of a simulated solar irradiation (Figure 6): a higher photocurrent value indicates a higher photoelectron yield. The trend of the photocurrent response ( $\text{Mo}_x\text{C}/\text{TiO}_2(\text{bipy}) \gg \text{TiO}_2(\text{bipy}) \gg \text{Mo}_x\text{C}/\text{TiO}_2(\text{NS})\text{-600} > \text{Mo}_x\text{C}/\text{TiO}_2(\text{NS})\text{-F} > \text{TiO}_2(\text{NS})\text{-600} > \text{TiO}_2(\text{NS})\text{-F}$ ) shows that the shape of  $\text{TiO}_2$  is of paramount importance.  $\text{Mo}_x\text{C}/\text{TiO}_2(\text{bipy})$  and  $\text{TiO}_2(\text{bipy})$  with bipyramidal  $\text{TiO}_2$  NPs showed much larger photocurrent density values than the other samples based on  $\text{TiO}_2$  NPs with nano-sheet morphology. Although in general an increase of the photocurrent density was found when  $\text{Mo}_x\text{C}$  is deposited onto  $\text{TiO}_2$ , this effect was much higher for bipyramidal  $\text{TiO}_2$  NPs.

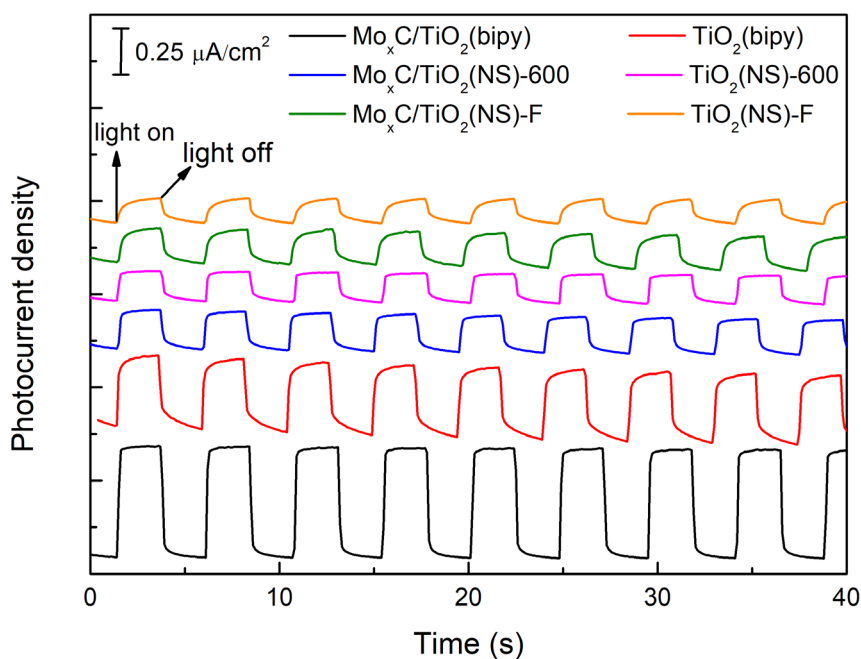


**Figure 6.** Photocurrent response of  $\text{Mo}_x\text{C}/\text{TiO}_2(\text{NS})\text{-X}$ ,  $\text{Mo}_x\text{C}/\text{TiO}_2(\text{bipy})$ ,  $\text{TiO}_2(\text{NS})\text{-X}$  and  $\text{TiO}_2(\text{bipy})$  samples.

For a better assessment of the electrochemical properties, all samples were also characterized by EIS both in dark conditions and under simulated solar irradiation. Figures 7A and 7B display the EIS Nyquist plots in dark and under irradiation, respectively. In all cases, the arc radius in dark conditions was larger than under illumination, being the order:  $\text{TiO}_2(\text{NS})\text{-F} > \text{TiO}_2(\text{NS})\text{-600} > \text{Mo}_x\text{C}/\text{TiO}_2(\text{NS})\text{-600} > \text{Mo}_x\text{C}/\text{TiO}_2(\text{NS})\text{-F} > \text{TiO}_2(\text{bipy}) > \text{Mo}_x\text{C}/\text{TiO}_2(\text{bipy})$ . For all  $\text{TiO}_2$  NPs, a decrease of the transport resistance of photoelectrons takes place after the  $\text{Mo}_x\text{C}$  deposition.

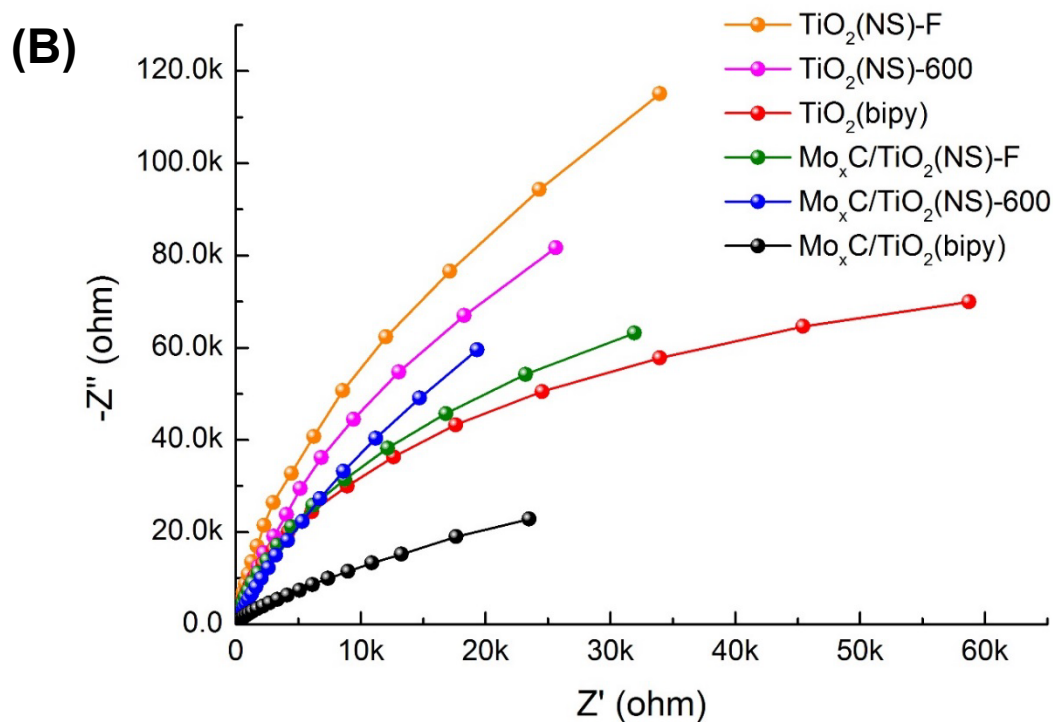
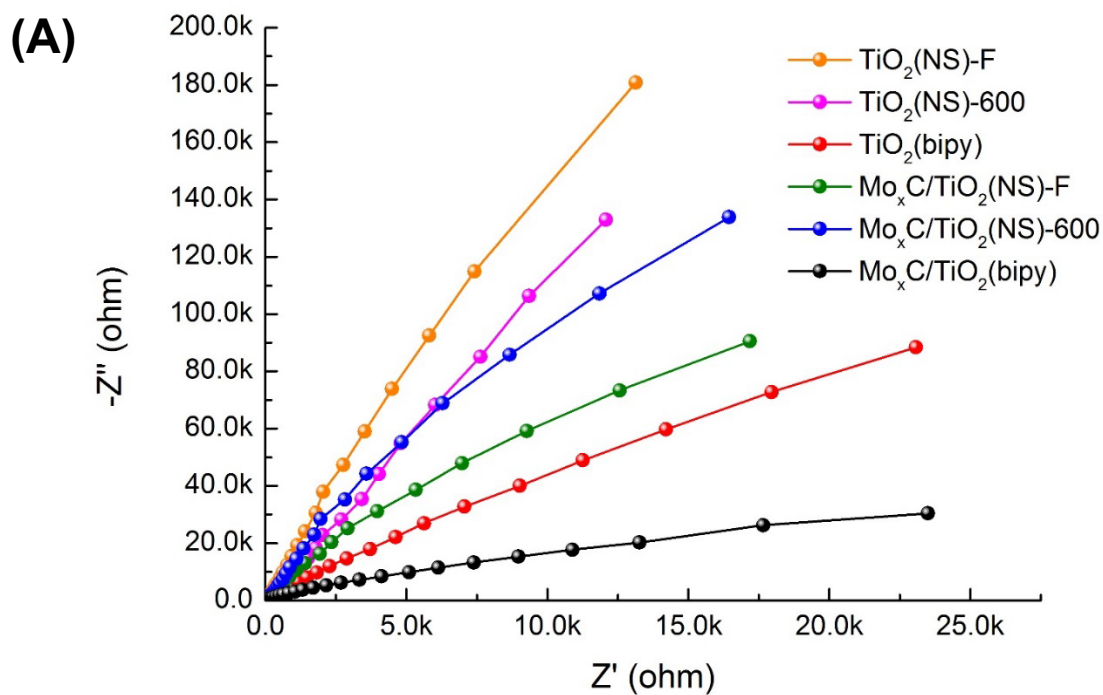
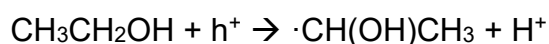


**Figure 7.** EIS Nyquist plots of  $\text{Mo}_x\text{C}/\text{TiO}_2(\text{NS})\text{-X}$ ,  $\text{Mo}_x\text{C}/\text{TiO}_2(\text{bipy})$ ,  $\text{TiO}_2(\text{NS})\text{-X}$  and  $\text{TiO}_2(\text{bipy})$  samples: A) in dark; B) under simulated solar irradiation.

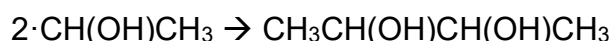
As stated above, all catalysts were tested in the photocatalytic H<sub>2</sub> production using aqueous ethanol (25%v/v) as sacrificial electron donor. Besides H<sub>2</sub>, small amounts of carbon containing products such as CO, CO<sub>2</sub>, methane, ethylene and acetaldehyde were detected in the gas phase (Table S2), while no O<sub>2</sub> was detected. On the other hand, 2,3-butanediol was the main product of ethanol transformation found in the liquid phase (Table S2).

As stated in the introduction section, once the electron/hole pairs are formed, a preferable migration of holes to {001} facets of TiO<sub>2</sub> and the migration of electrons to {101} facets will take place [58]. In particular, DFT calculations showed that, after the formation of a delocalized hole in the valence band and a delocalized electron in the conduction band, structural relaxation induces localization of the hole on a single surface O ion of the (001) surface and migration of the excited electron at the (101) surface, where it localizes to form a Ti<sup>3+</sup> ion [59].

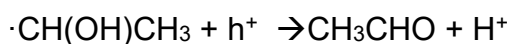
The photogenerated holes are proposed to produce the first oxidation step of ethanol with the α-hydroxyethyl radical formation [60]:



The formation of 2,3-butanediol from the ethanol photo-transformation has been proposed via the coupling of two α-hydroxyethyl radicals:



A subsequent oxidation of α-hydroxyethyl will produce acetaldehyde [60]:



Meanwhile, the reduction process will take place mainly over the {101} facets, where the electrons can be transferred to the Mo<sub>x</sub>C NPs and then to adsorbed protons, leading to hydrogen evolution:



Figure 8 shows the values of H<sub>2</sub> production for bare TiO<sub>2</sub> samples and Mo<sub>x</sub>C/TiO<sub>2</sub> materials. For comparison, a catalytic test was also carried out with reference TiO<sub>2</sub> P25, which showed the poorest photocatalytic behavior. As visible in Figure 8, for bare TiO<sub>2</sub> samples the H<sub>2</sub> production yield followed the order TiO<sub>2</sub>(bipy) > TiO<sub>2</sub>(NS)-600 > TiO<sub>2</sub>(NS)-F, which confirms

the importance of the TiO<sub>2</sub> nanoparticle shape in the H<sub>2</sub> production reaction. A similar trend has been recently found for the formic acid photoreforming [20]. Indeed, the overwhelming presence of exposed {101} facets in bipyramidal anatase favors the electron transfer necessary for the H<sub>2</sub> production, as it has been also demonstrated for the hydrogen production from methanolic solutions [61]. Moreover, in all cases, the presence of Mo<sub>x</sub>C onto TiO<sub>2</sub> increased the H<sub>2</sub> production. However, this effect was higher for bipyramidal TiO<sub>2</sub> NPs. Indeed, Mo<sub>x</sub>C/TiO<sub>2</sub>(bipy) showed the highest photocurrent response, the lowest electron/hole recombination rate and the lowest transport resistance of photoelectrons. We relate the highest co-catalyst effect of Mo<sub>x</sub>C on TiO<sub>2</sub>(bipy) with the presence of Mo<sub>x</sub>C nanoparticles onto {101} facets, which accelerates the electron transfer, decreasing the rate of electron/hole recombination and thus increasing the hydrogen yield.

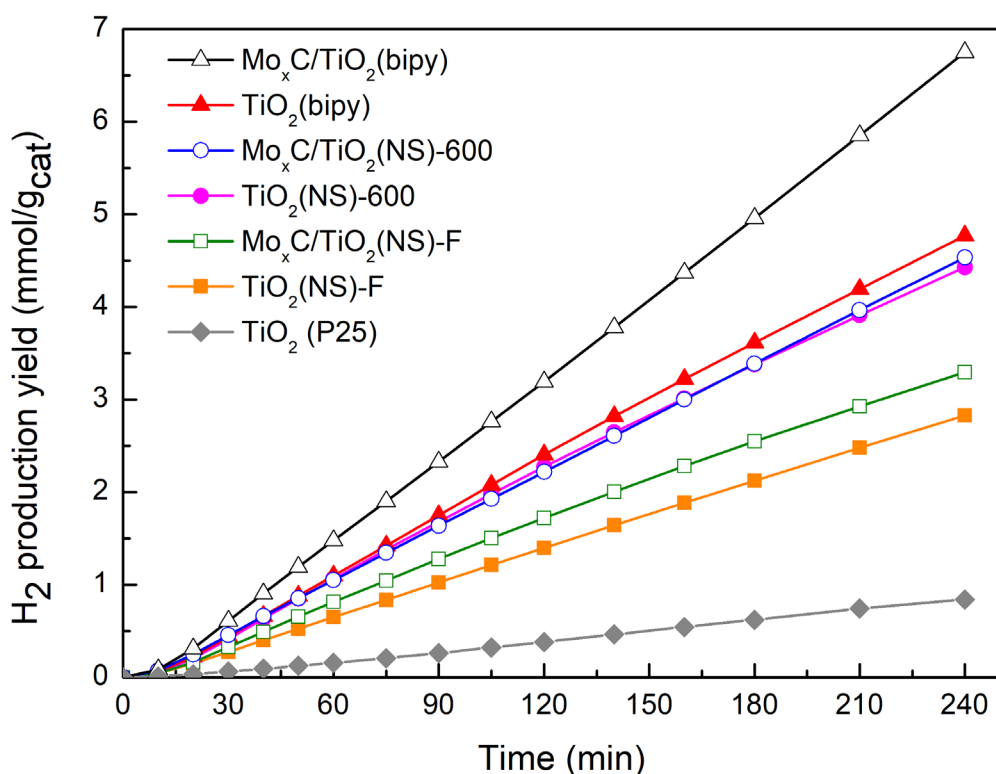


**Figure 8.** Photocatalytic H<sub>2</sub> production from 25%v/v ethanol<sub>(aq)</sub> using Mo<sub>x</sub>C/TiO<sub>2</sub>(NS)-X, Mo<sub>x</sub>C/TiO<sub>2</sub>(bipy), TiO<sub>2</sub>(NS)-X and TiO<sub>2</sub>(bipy) samples; t = 4h, T = 20 °C. The results for TiO<sub>2</sub> P25 are also reported as benchmark.

To further assess the photocatalytic behavior and the stability of the  $\text{Mo}_x\text{C}/\text{TiO}_2$  systems, in Figure 9A we report the  $\text{H}_2$  production rate along time for the different catalysts. For  $\text{Mo}_x\text{C}/\text{TiO}_2(\text{NS})$ -600 and  $\text{Mo}_x\text{C}/\text{TiO}_2(\text{bipy})$ , the rate of photoproduction of hydrogen is rather stable after the first 30 min: in both cases, the rate of  $\text{H}_2$  production after the initial stabilization time (30 min) and at the end of the catalytic test (4 h) differ only in a 5%. Moreover, for the most performant system,  $\text{Mo}_x\text{C}/\text{TiO}_2(\text{bipy})$ , a reusability test was carried out (Figure 9B), highlighting a similar photocatalytic behavior of fresh and used catalyst.

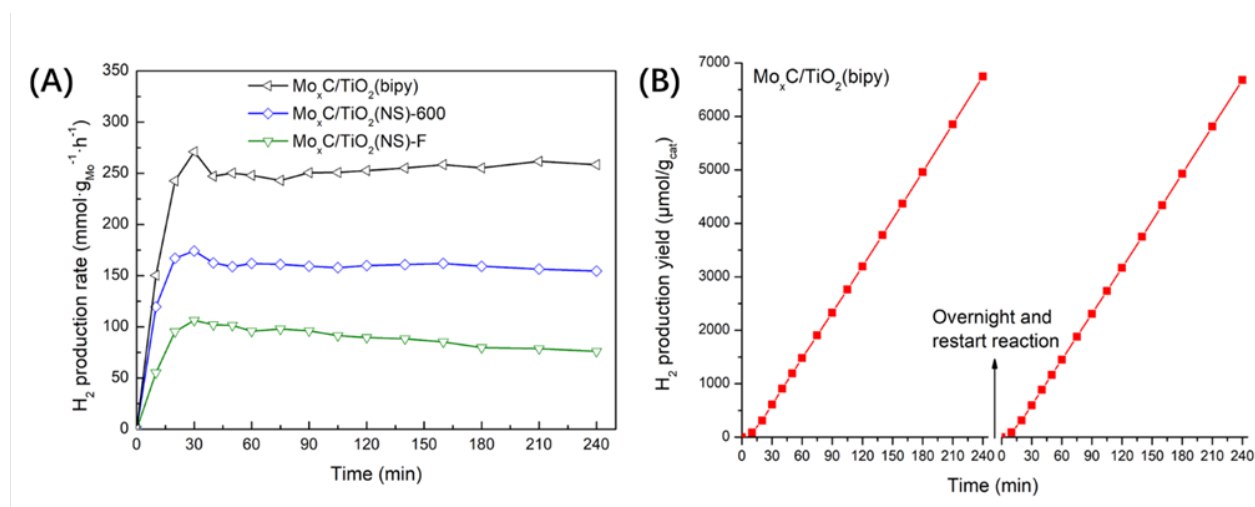


**Figure 9.** A) Variation of the  $\text{H}_2$  production rate along time, during the photocatalytic test using 25%v/v ethanol<sub>(aq)</sub> and  $\text{Mo}_x\text{C}/\text{TiO}_2(\text{NS})$ -X or  $\text{Mo}_x\text{C}/\text{TiO}_2(\text{bipy})$  samples; T = 20 °C. B) Photocatalytic  $\text{H}_2$  production from 25%v/v ethanol<sub>(aq)</sub> in two consecutive tests using  $\text{Mo}_x\text{C}/\text{TiO}_2(\text{bipy})$ .

#### 4. Conclusions

$\text{Mo}_x\text{C}/\text{TiO}_2$  photocatalysts were prepared combining previously synthesized  $\text{Mo}_x\text{C}$  NPs, as co-catalyst, and three kinds of shape-controlled anatase  $\text{TiO}_2$  NPs exposing different percentages of {101} and {001} facets.  $\text{Mo}_x\text{C}$  NPs, which were deposited by an ultrasonic treatment, were constituted by 86% of fcc MoC and 14 % of hcp Mo<sub>2</sub>C with average size of 4-6 and 11-12 nm, respectively. In the bipyramidal anatase samples, the deposition of  $\text{Mo}_x\text{C}$

on TiO<sub>2</sub>, likely induced a preferential reduction of Ti<sup>4+</sup> of the dominant {101} facets, which resulted in the formation of surface Ti<sup>3+</sup> species.

The photoelectrochemical characterization of the photocatalysts indicated that the presence of Mo<sub>x</sub>C onto TiO<sub>2</sub> NPs increases the photoelectron yield and photocurrent response and decreases the electron/hole recombination rate. These effects were higher for bipyramidal TiO<sub>2</sub> than for nano-sheet TiO<sub>2</sub>.

The presence of the Mo<sub>x</sub>C NPs clearly increased the reaction yields of photocatalytic H<sub>2</sub> formation, confirming that carbide phases are promising co-catalysts of TiO<sub>2</sub> to prepare efficient noble metal-free photocatalysts based on TiO<sub>2</sub>. The efficiency of the final system is correlated with the TiO<sub>2</sub> NPs shape and, in particular, with the amount of {101} facets present. The proposed mechanism involves, after charge carriers photogeneration, the migration of the holes to the {001} facets where they can oxidize adsorbed ethanol, generating different carbon-containing products. In parallel, the electrons migrate to the {101} facets where they are transferred to the Mo<sub>x</sub>C NPs, increasing the lifetime of the electron-hole couple, and then to adsorbed protons to generate H<sub>2</sub>.

## **Acknowledgements**

L. M. thanks the Italian Ministry of Education, University and Research (MIUR) for supporting his stay at the Universitat de Barcelona through the “Leonardo da Vinci 2019” action. N.H. and P.R.P thank the MAT2017-87500-P and PID2020-116031RB-I00 projects from MCIN/AEI/10.13039/501100011033/FEDER for financial support. Y. W. thanks the China scholarship Council for his PhD grant CSC201608460014. Dr. Vasile-Dan Hodoroba is acknowledged for the acquisition of the SEM images.

## References

- [1] X.B. Chen, S.H. Shen, L.J. Guo, S.S. Mao, Semiconductor-based Photocatalytic Hydrogen Generation *Chem. Rev.* 110 (2010) 6503-6570.
- [2] N. Fajrina, M. Tahir, A critical review in strategies to improve photocatalytic water splitting towards hydrogen production *Int. J. Hydrog. Energy* 44 (2019) 540-577.
- [3] D.Y.C. Leung, X.L. Fu, C.F. Wang, M. Ni, M.K.H. Leung, X.X. Wang, X.Z. Fu, Hydrogen Production over Titania-Based Photocatalysts *ChemSusChem* 3 (2010) 681-694.
- [4] S.M. Jain, J.J. Biedrzycki, V. Maurino, A. Zecchina, L. Mino, G. Spoto, Acetylene oligomerization on the surface of TiO<sub>2</sub>: a step forward in the in situ synthesis of nanostructured carbonaceous structures on the surface of photoactive oxides *J. Mater. Chem. A* 2 (2014) 12247-12254.
- [5] Y. Ma, X.L. Wang, Y.S. Jia, X.B. Chen, H.X. Han, C. Li, Titanium Dioxide-Based Nanomaterials for Photocatalytic Fuel Generations *Chem. Rev.* 114 (2014) 9987-10043.
- [6] G. Liu, J.C. Yu, G.Q. Lu, H.M. Cheng, Crystal facet engineering of semiconductor photocatalysts: motivations, advances and unique properties *Chem. Commun.* 47 (2011) 6763-6783.
- [7] S. Bai, L.L. Wang, Z.Q. Li, Y.J. Xiong, Facet-Engineered Surface and Interface Design of Photocatalytic Materials *Adv. Sci.* 4 (2017) 26.
- [8] H.G. Yang, C.H. Sun, S.Z. Qiao, J. Zou, G. Liu, S.C. Smith, H.M. Cheng, G.Q. Lu, Anatase TiO<sub>2</sub> single crystals with a large percentage of reactive facets *Nature* 453 (2008) 638-641.
- [9] L. Mino, A.M. Ferrari, V. Lacivita, G. Spoto, S. Bordiga, A. Zecchina, CO Adsorption on Anatase Nanocrystals: A Combined Experimental and Periodic DFT Study *J. Phys. Chem. C* 115 (2011) 7694-7700.
- [10] L. Mino, G. Spoto, S. Bordiga, A. Zecchina, Particles Morphology and Surface Properties As Investigated by HRTEM, FTIR, and Periodic DFT Calculations: From Pyrogenic TiO<sub>2</sub> (P25) to Nanoanatase *J. Phys. Chem. C* 116 (2012) 17008-17018.
- [11] L. Mino, A. Zecchina, G. Martra, A.M. Rossi, G. Spoto, A surface science approach to TiO<sub>2</sub> P25 photocatalysis: An in situ FTIR study of phenol photodegradation at controlled water coverages from sub-monolayer to multilayer *Appl. Catal. B-Environ.* 196 (2016) 135-141.
- [12] L. Mino, C. Negri, R. Santalucia, G. Cerrato, G. Spoto, G. Martra, Morphology, Surface Structure and Water Adsorption Properties of TiO<sub>2</sub> Nanoparticles: A Comparison of Different Commercial Samples *Molecules* 25 (2020) 4605.
- [13] M. Liu, L.Y. Piao, L. Zhao, S.T. Ju, Z.J. Yan, T. He, C.L. Zhou, W.J. Wang, Anatase TiO<sub>2</sub> single crystals with exposed {001} and {110} facets: facile synthesis and enhanced photocatalysis *Chem. Commun.* 46 (2010) 1664-1666.
- [14] J. Pan, G. Liu, G.M. Lu, H.M. Cheng, On the True Photoreactivity Order of {001}, {010}, and {101} Facets of Anatase TiO<sub>2</sub> Crystals *Angew. Chem.-Int. Edit.* 50 (2011) 2133-2137.
- [15] M. Maisano, M.V. Dozzi, M. Coduri, L. Artiglia, G. Granozzi, E. Selli, Unraveling the Multiple Effects Originating the Increased Oxidative Photoactivity of {001}-Facet Enriched Anatase TiO<sub>2</sub> *ACS Appl. Mater. Interfaces* 8 (2016) 9745-9754.

- [16] M. Dozzi, E. Selli, Specific Facets-Dominated Anatase TiO<sub>2</sub>: Fluorine-Mediated Synthesis and Photoactivity Catalysts 3 (2013) 455-485.
- [17] L.Q. Ye, J. Mao, J.Y. Liu, Z. Jiang, T.Y. Peng, L. Zan, Synthesis of anatase TiO<sub>2</sub> nanocrystals with {101}, {001} or {010} single facets of 90% level exposure and liquid-phase photocatalytic reduction and oxidation activity orders J. Mater. Chem. A 1 (2013) 10532-10537.
- [18] H. Xu, S.X. Ouyang, P. Li, T. Kako, J.H. Ye, High-Active Anatase TiO<sub>2</sub> Nanosheets Exposed with 95% {100} Facets Toward Efficient H<sub>2</sub> Evolution and CO<sub>2</sub> Photoreduction ACS Appl. Mater. Interfaces 5 (2013) 1348-1354.
- [19] M. D'Arienzo, M.V. Dozzi, M. Redaelli, B. Di Credico, F. Morazzoni, R. Scotti, S. Polizzi, Crystal Surfaces and Fate of Photogenerated Defects in Shape-Controlled Anatase Nanocrystals: Drawing Useful Relations to Improve the H<sub>2</sub> Yield in Methanol Photosteam Reforming J. Phys. Chem. C 119 (2015) 12385-12393.
- [20] F. Pellegrino, F. Sordello, L. Mino, C. Minero, V.D. Hodoroaba, G. Martra, V. Maurino, Formic Acid Photoreforming for Hydrogen Production on Shape-Controlled Anatase TiO<sub>2</sub> Nanoparticles: Assessment of the Role of Fluorides, {101}/{001} Surfaces Ratio, and Platinization ACS Catal. 9 (2019) 6692-6697.
- [21] M.V. Dozzi, M. Montalbano, G. Marra, L. Mino, E. Selli, Effects of anatase TiO<sub>2</sub> morphology and surface fluorination on environmentally relevant photocatalytic reduction and oxidation reactions Mater. Today Chem. 22 (2021) 11.
- [22] F. Sordello, F. Pellegrino, M. Prozzi, C. Minero, V. Maurino, Controlled Periodic Illumination Enhances Hydrogen Production by over 50% on Pt/TiO<sub>2</sub> ACS Catal. 11 (2021) 6484-6488.
- [23] S.B. Patil, P.S. Basavarajappa, N. Ganganagappa, M.S. Jyothi, A.V. Raghu, K.R. Reddy, Recent advances in non-metals-doped TiO<sub>2</sub> nanostructured photocatalysts for visible-light driven hydrogen production, CO<sub>2</sub> reduction and air purification Int. J. Hydrog. Energy 44 (2019) 13022-13039.
- [24] B.J. Ma, H.J. Xu, K.Y. Lin, J. Li, H.J. Zhan, W.Y. Liu, C. Li, Mo<sub>2</sub>C as Non-Noble Metal Co-Catalyst in Mo<sub>2</sub>C/CdS Composite for Enhanced Photocatalytic H<sub>2</sub> Evolution under Visible Light Irradiation ChemSusChem 9 (2016) 820-824.
- [25] L. Tian, S.X. Min, Y.G. Lei, S.S. Chen, F. Wang, Vanadium carbide: an efficient, robust, and versatile cocatalyst for photocatalytic hydrogen evolution under visible light Chem. Commun. 55 (2019) 6870-6873.
- [26] A. Pajares, H. Prats, A. Romero, F. Vines, P. Ramirez de la Piscina, R. Sayos, N. Homs, F. Illas, Critical effect of carbon vacancies on the reverse water gas shift reaction over vanadium carbide catalysts Appl. Catal. B-Environ. 267 (2020) 10.
- [27] S. Ahmad, I. Ashraf, M.A. Mansoor, S. Rizwan, M. Iqbal, An Overview of Recent Advances in the Synthesis and Applications of the Transition Metal Carbide Nanomaterials Nanomaterials 11 (2021) 34.
- [28] P.M. Patterson, T.K. Das, B.H. Davis, Carbon monoxide hydrogenation over molybdenum and tungsten carbides Appl. Catal. A-Gen. 251 (2003) 449-455.
- [29] W.F. Chen, C.H. Wang, K. Sasaki, N. Marinkovic, W. Xu, J.T. Muckerman, Y. Zhu, R.R. Adzic, Highly active and durable nanostructured molybdenum carbide electrocatalysts for hydrogen production Energy Environ. Sci. 6 (2013) 943-951.

- [30] A.T. Garcia-Esparza, D. Cha, Y.W. Ou, J. Kubota, K. Domen, K. Takahashi, Tungsten Carbide Nanoparticles as Efficient Cocatalysts for Photocatalytic Overall Water Splitting *ChemSusChem* 6 (2013) 168-181.
- [31] X.Y. Liu, C. Kunkel, P. Ramirez de la Piscina, N. Homs, F. Vines, F. Illas, Effective and Highly Selective CO Generation from CO<sub>2</sub> Using a Polycrystalline  $\alpha$ -Mo<sub>2</sub>C Catalyst *ACS Catal.* 7 (2017) 4323-4335.
- [32] W. Liu, B.X. Chen, X.Z. Duan, K.H. Wu, W. Qi, X.L. Guo, B.S. Zhang, D.S. Su, Molybdenum Carbide Modified Nanocarbon Catalysts for Alkane Dehydrogenation Reactions *ACS Catal.* 7 (2017) 5820-5827.
- [33] A. Pajares, Y. Wang, M.J. Kronenberg, P. Ramirez de la Piscina, N. Homs, Photocatalytic H<sub>2</sub> production from ethanol aqueous solution using TiO<sub>2</sub> with tungsten carbide nanoparticles as co-catalyst *Int. J. Hydrog. Energy* 45 (2020) 20558-20567.
- [34] L.L. Gao, J.F. Liu, H.Y. Long, P. Wang, H.G. Yu, One-step calcination synthesis of WC-Mo<sub>2</sub>C heterojunction nanoparticles as novel H<sub>2</sub>-production cocatalysts for enhanced photocatalytic activity of TiO<sub>2</sub> *Catal. Sci. Technol.* 11 (2021) 7307-7315.
- [35] X.Y. Zhang, J.C. Wang, T. Guo, T.Y. Liu, Z.Z. Wu, L. Cavallo, Z. Cao, D.Z. Wang, Structure and phase regulation in Mo<sub>x</sub>C ( $\alpha$ -MoC<sub>1-x</sub>/ $\beta$ -Mo<sub>2</sub>C) to enhance hydrogen evolution *Appl. Catal. B-Environ.* 247 (2019) 78-85.
- [36] P. Ramirez de la Piscina, N. Homs, Use of biofuels to produce hydrogen (reformation processes) *Chem. Soc. Rev.* 37 (2008) 2459-2467.
- [37] L.V. Mattos, G. Jacobs, B.H. Davis, F.B. Noronha, Production of Hydrogen from Ethanol: Review of Reaction Mechanism and Catalyst Deactivation *Chem. Rev.* 112 (2012) 4094-4123.
- [38] X.G. Han, Q. Kuang, M.S. Jin, Z.X. Xie, L.S. Zheng, Synthesis of Titania Nanosheets with a High Percentage of Exposed (001) Facets and Related Photocatalytic Properties *J. Am. Chem. Soc.* 131 (2009) 3152-3153.
- [39] F. Pellegrino, E. Morra, L. Mino, G. Martra, M. Chiesa, V. Maurino, Surface and Bulk Distribution of Fluorides and Ti<sup>3+</sup> Species in TiO<sub>2</sub> Nanosheets: Implications on Charge Carrier Dynamics and Photocatalysis *J. Phys. Chem. C* 124 (2020) 3141-3149.
- [40] F. Pellegrino, R. Isopescu, L. Pellutic, F. Sordello, A.M. Rossi, E. Ortel, G. Martra, V.D. Hodoroaba, V. Maurino, Machine learning approach for elucidating and predicting the role of synthesis parameters on the shape and size of TiO<sub>2</sub> nanoparticles *Sci Rep* 10 (2020) 11.
- [41] X.Y. Liu, A. Pajares, D. Matienzo, P. Ramirez de la Piscina, N. Homs, Preparation and characterization of bulk Mo<sub>x</sub>C catalysts and their use in the reverse water-gas shift reaction *Catal. Today* 356 (2020) 384-389.
- [42] R.L. Snyder, The Use of Reference Intensity Ratios in X-Ray Quantitative Analysis *Powder Diffr.* 7 (1992) 186-193.
- [43] P. Makula, M. Pacia, W. Macyk, How To Correctly Determine the Band Gap Energy of Modified Semiconductor Photocatalysts Based on UV-Vis Spectra *J. Phys. Chem. Lett.* 9 (2018) 6814-6817.
- [44] L. Mino, F. Pellegrino, S. Rades, J. Radnik, V.D. Hodoroaba, G. Spoto, V. Maurino, G. Martra, Beyond Shape Engineering of TiO<sub>2</sub> Nanoparticles: Post-Synthesis Treatment Dependence of Surface Hydration, Hydroxylation, Lewis Acidity and Photocatalytic Activity

of TiO<sub>2</sub> Anatase Nanoparticles with Dominant {001} or {101} Facets ACS Appl. Nano Mater. 1 (2018) 5355-5365.

[45] X.H. Yang, Z. Li, C.H. Sun, H.G. Yang, C.Z. Li, Hydrothermal Stability of {001} Faceted Anatase TiO<sub>2</sub> Chem. Mat. 23 (2011) 3486-3494.

[46] A. Shrestha, X.T. Gao, J.C. Hicks, C. Paolucci, Nanoparticle Size Effects on Phase Stability for Molybdenum and Tungsten Carbides Chem. Mat. 33 (2021) 4606-4620.

[47] J.D. Zhu, E.A.A. Uslamin, N. Kosinov, E.J.M. Hensen, Tuning the reactivity of molybdenum (oxy)carbide catalysts by the carburization degree: CO<sub>2</sub> reduction and anisole hydrodeoxygenation Catal. Sci. Technol. 10 (2020) 3635-3645.

[48] M.D. Porosoff, X.F. Yang, J.A. Boscoboinik, J.G.G. Chen, Molybdenum Carbide as Alternative Catalysts to Precious Metals for Highly Selective Reduction of CO<sub>2</sub> to CO Angew. Chem.-Int. Edit. 53 (2014) 6705-6709.

[49] G. Liu, H.G. Yang, X.W. Wang, L.N. Cheng, H.F. Lu, L.Z. Wang, G.Q. Lu, H.M. Cheng, Enhanced Photoactivity of Oxygen-Deficient Anatase TiO<sub>2</sub> Sheets with Dominant {001} Facets J. Phys. Chem. C 113 (2009) 21784-21788.

[50] A.C. Sola, P. Ramirez de la Piscina, N. Homs, Behaviour of Pt/TiO<sub>2</sub> catalysts with different morphological and structural characteristics in the photocatalytic conversion of ethanol aqueous solutions Catal. Today 341 (2020) 13-20.

[51] S. Selcuk, X.H. Zhao, A. Selloni, Structural evolution of titanium dioxide during reduction in high-pressure hydrogen Nat. Mater. 17 (2018) 923-928.

[52] V. Luca, Comparison of Size-Dependent Structural and Electronic Properties of Anatase and Rutile Nanoparticles J. Phys. Chem. C 113 (2009) 6367-6380.

[53] J.Y. Shi, J. Chen, Z.C. Feng, T. Chen, Y.X. Lian, X.L. Wang, C. Li, Photoluminescence characteristics of TiO<sub>2</sub> and their relationship to the photoassisted reaction of water/methanol mixture J. Phys. Chem. C 111 (2007) 693-699.

[54] R. Bruninghoff, K. Wenderich, J.P. Korterik, B.T. Mei, G. Mul, A. Huijser, Time-Dependent Photoluminescence of Nanostructured Anatase TiO<sub>2</sub> and the Role of Bulk and Surface Processes J. Phys. Chem. C 123 (2019) 26653-26661.

[55] W.T. Li, C.L. Shang, X. Li, A one-step thermal decomposition method to prepare anatase TiO<sub>2</sub> nanosheets with improved adsorption capacities and enhanced photocatalytic activities Appl. Surf. Sci. 357 (2015) 2223-2233.

[56] D.K. Pallotti, L. Passoni, P. Maddalena, F. Di Fonzo, S. Lettieri, Photoluminescence Mechanisms in Anatase and Rutile TiO<sub>2</sub> J. Phys. Chem. C 121 (2017) 9011-9021.

[57] L.Q. Jing, Y.C. Qu, B.Q. Wang, S.D. Li, B.J. Jiang, L.B. Yang, W. Fu, H.G. Fu, J.Z. Sun, Review of photoluminescence performance of nano-sized semiconductor materials and its relationships with photocatalytic activity Sol. Energy Mater. Sol. Cells 90 (2006) 1773-1787.

[58] N. Murakami, Y. Kurihara, T. Tsubota, T. Ohno, Shape-Controlled Anatase Titanium(IV) Oxide Particles Prepared by Hydrothermal Treatment of Peroxo Titanic Acid in the Presence of Polyvinyl Alcohol J. Phys. Chem. C 113 (2009) 3062-3069.

[59] G. Di Liberto, S. Tosoni, G. Pacchioni, Role of Heterojunction in Charge Carrier Separation in Coexposed Anatase (001)-(101) Surfaces J. Phys. Chem. Lett. 10 (2019) 2372-2377.

- [60] H.Q. Lu, J.H. Zhao, L. Li, L.M. Gong, J.F. Zheng, L.X. Zhang, Z.J. Wang, J. Zhang, Z.P. Zhu, Selective oxidation of sacrificial ethanol over TiO<sub>2</sub>-based photocatalysts during water splitting *Energy Environ. Sci.* 4 (2011) 3384-3388.
- [61] T.R. Gordon, M. Cargnello, T. Paik, F. Mangolini, R.T. Weber, P. Fornasiero, C.B. Murray, Nonaqueous Synthesis of TiO<sub>2</sub> Nanocrystals Using TiF<sub>4</sub> to Engineer Morphology, Oxygen Vacancy Concentration, and Photocatalytic Activity *J. Am. Chem. Soc.* 134 (2012) 6751-6761.